Contrib Mineral Petrol (2000) 140: 283–295

Leander Franz · Richard Wirth

Spinel inclusions in olivine of peridotite xenoliths from TUBAF seamount (Bismarck Archipelago/Papua New Guinea): evidence for the thermal and tectonic evolution of the oceanic lithosphere

Received: 25 May 2000 / Accepted: 12 July 2000

Abstract Olivine in spinel peridotite xenoliths from the Bismarck Archipelago northeast of Papua New Guinea, which were transported to the surface by Quaternary basalts, shows spinel inclusions up to 25 μm long and 200 nm wide. These inclusions mainly occur as inhomogeneously distributed needles and subordinately as octahedral grains in olivine of veined metasomatic peridotites as well as peridotites without obvious metasomatism. The needles very often occur in swarms with irregular spacing in between them. Similar spinel inclusions in olivine have only previously been reported from ultramafites of meteoritic origin. Composition and orientation of the spinel inclusions were determined by transmission electron microscopy (TEM) and analytical electron microscopy (AEM). Both the needles and the grains display a uniform crystallographic orientation in the host olivine with $[001]_{Ol}//[1\bar{1}0]_{Spl}$ and $(100)_{Ol}//(111)_{Spl}$. The needles are elongated parallel [010] in olivine, which is the same in all olivine grains. As these needles have no relation to the metasomatic sections in the peridotite, it is concluded that they are primary features of the rock. Although the composition of the spinel needles is often very similar to the large chromian spinel octahedra in the matrix, the small octahedral spinel inclusions in olivine are in part Mg-rich aluminous spinel and sometimes almost pure magnetite. The spinel needles are suggested to have formed by exsolution processes during cooling of Al- and Cr-rich, high-temperature olivine during the initial formation of the lithospheric mantle at the mid-ocean ridge. The Al-rich spinel octahedra probably formed by the breakdown of an Al-rich phase such as phlogopite or by metasomatism, whereas the magnetite was generated by oxidizing fluids. These oxidizing fluids may either have been set free by dehydration of the underlying, subducted plate or by the Quaternary magmatism responsible for the transport of the xenoliths to the seafloor.

L. Franz (✉)
Institut für Mineralogie, TU Bergakademie Freiberg,
Brennhausgasse 14, 09596 Freiberg, Germany
e-mail: lfranz@mineral.tu-freiberg.de

R. Wirth
GeoForschungsZentrum Potsdam,
Telegrafenberg, 14473 Potsdam, Germany

Editorial responsibility: J. Hoefs

Introduction

Inclusions are a common feature in olivine of mantle peridotites and in magmatic olivine; numerous types of symplectitic exsolutions of spinel, ortho- and clinopyroxene are described in literature (Bell et al. 1975; Arai 1978; Putnis 1979; Moseley 1984; Puga et al. 1999). Similar observations of needles in olivine are reported from several rock types. Needle-shaped lamellae of chromian spinel and clinopyroxene were detected in olivine from the Iwanai-Dake peridotite mass in Japan (Arai 1978), and lamellae of kirschsteinite ($CaFeSiO_4$) were found in olivine of the angrite meteorite (Mikouchi et al. 1995). Magnetite lamellae in olivine and clinohumite were described from ultrahigh-pressure metamorphic rocks from the Dabie Shan in China (Zhang et al. 1999) and needles of magnetite and clinopyroxene were reported from intrusive rocks from Greenland (Markl et al. 2000). Coupled exsolutions of chromian spinel and CO_2 (and sometimes native carbon) may occur in olivine from mantle xenoliths (Green and Gueguen 1983; Green 1985). Most of these inclusions are interpreted as exsolutions because of decompression, cooling or oxidation processes. In natural rocks, inclusions commonly form polyphase assemblages consisting of spinel, pyroxenes and/or a fluid phase. Descriptions of single-phase chromian or aluminous spinel inclusions in olivine are rare and limited to chondritic meteorites (Ashworth 1979). We report here on tiny spinel needles and octahedral grains embedded in olivine of mantle peridotite xenoliths from the TUBAF seamount in the Bismarck Archipelago, northeast of Papua New Guinea. Electron microprobe and transmission electron microscope (TEM, AEM) investigations reveal the composition and the crystallographic orientation of these inclusions in the host olivine and allow an interpretation of their formation.

Geological setting

The Bismarck Archipelago northeast of the island of Papua New Guinea comprises the islands of the New Britain arc-trench system, New Ireland, New Hanover, Bougainville and the Solomons (Fig. 1). The archipelago is underlain by the Bismarck microplate, which was generated in a mid-ocean ridge (MOR) environment (McInnes et al. 1999). In this area, the Pacific plate in the NE underwent subduction below the Bismarck microplate in the SW along the so called Manus–Kilinailau trench. The subduction, which was accompanied by strong calc-alkaline volcanism in Oligocene and Miocene, was stopped ~15 Ma ago, when a collision of the Ontong–Java plateau with the trench occurred (Coleman and Kroenke 1981). The stalling of the subduction zone resulted in the development of a subduction reversal leading to the formation of the New Britain trench, on which a northward subduction of the Solomon Sea microplate under the South Bismarck microplate is presently taking place (see Fig. 1; McInnes and Cameron 1994).

The island of Lihir belongs to the NW–SE trending Tabar–Lihir–Tanga–Feni volcanic island chain extending for a distance of more than 250 km northeast of New Ireland. Volcanic activity started ~3.6 Ma ago in the New Ireland fore-arc region and continues until now (Licence et al. 1987; McInnes 1992; Rytuba et al. 1993). The high-K calc-alkaline volcanism can be related to lithospheric extension along NE-trending faults (Taylor 1979; Steward and Sandy 1988) and incorporates alkali-olivine basalts, trachybasalts, trachyandesites, ankaramites and foid-bearing mafites (Wallace et al. 1983; Kennedy et al. 1990). These melts were generated as a consequence of the thinning of the New Ireland basin lithosphere and subsequent decompression. The magma genesis is strongly influenced by the stalled subduction along the Manus–Kilinailau trench. Metasomatizing agents from the underlying subducted Pacific plate penetrated the overlying mantle segment and induced the formation of veined mantle (McInnes and Cameron 1994; McInnes et al. 1999, 2000; Franz et al. 2000).

In the course of two cruises of the research vessel RV *Sonne*, 12 submarine volcanoes were mapped south of Lihir Island (Herzig et al. 1994, 1998). One of these volcanoes, the so called TUBAF seamount, is made up of pristine pyroclastic deposits and characterized by the absence of pelagic sediments indicating a relatively recent eruption. The ankaramitic magmatites of this volcano contain numerous fresh mantle xenoliths, which were sampled by video-guided grab. In many cases, the mantle peridotites gave evidence for vivid metasomatism in the form of pyroxene-, hornblende-, and phlogopite-bearing veins. A detailed description of the mineral assemblages, the vein-forming reactions and the geochemistry of these rocks has recently been performed (Franz et al. 2000).

Sample preparation and analytical details

Microprobe analyses were performed using a JEOL Superprobe with five spectrometers at the University of Freiberg. Major and minor elements were determined at 15 kV acceleration voltage and a beam current of 20 nA with counting times of 20 s for Si, Al, Mg, Ca, Sr, Ba and K, and 30 s for Fe, Ni, Na, Cr, Mn and Ti. Ca, Al and Cr in olivine were determined with an acceleration voltage of 20 kV, a beam current of 55 nA, and a counting time of 300 s on the peak. The standard sets of the Smithsonian Institute (cf. Jarosewich et al. 1980) and MAC were used for reference.

The TEM specimens were prepared from standard thin sections without a cover glass. The areas of interest were removed from the thin section, glued onto a copper grid and finally thinned with an ion beam (5 kV, 12° tilt of the ion guns). After thinning, the specimen were slightly coated with carbon to prevent charging.

TEM and AEM were carried out in a Philips CM200 operated at 200 kV. The electron source was a LaB_6 filament. The TEM is equipped with an EDAX X-ray analyzer with ultrathin window. The spectra were corrected for absorption and fluorescence and analysis totals normalized to 100%. The spectra were acquired in the scanning mode using a nominal beam diameter of 4 nm. To minimize irradiation damage the beam was scanned over an area of typically 40 × 30 nm in size. The counting time was 120–180 s, which gives sufficiently high counts to keep the error from counting statistics low. The k_{AB} factors were determined from measuring at least 20 different areas of the standard. Specimen thickness, necessary for absorption correction was determined by electron energy-loss spectroscopy (EELS) using the zero-loss peak and the whole spectrum (Egerton 1996). The EEL spectra were recorded with a Gatan GIF. The total error (error from k_{AB}-factor determination + the error from the counting statistics) is ~3% relative (rel.)

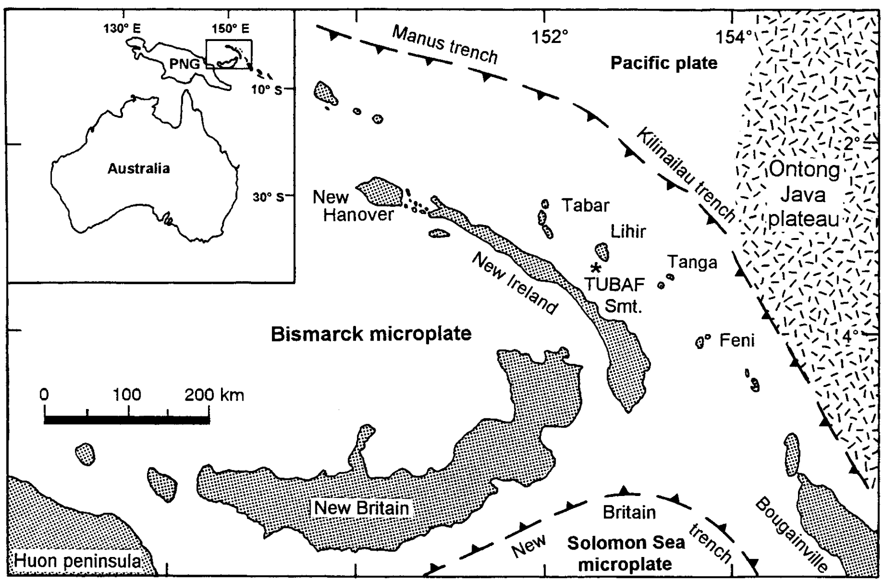

Fig. 1 Map of the Bismarck Archipelago with the position of the TUBAF seamount; *inset* shows the location of the area northeast of Papua New Guinea (PNG)

for MgO and SiO_2 and 7% rel. for FeO in olivine. For low elemental concentrations the total error might exceed 50% rel.

Element mapping of the spinel inclusions was performed with the GIF, applying the jump ratio or elemental mapping method of the Gatan Digital Micrograph software package.

Results

Petrography, mineral chemistry and thermobarometry of the xenoliths

Most of the mantle xenoliths are pristine spinel and plagioclase peridotites with coarse-equant textures following the classification of Harte (1975). Especially the spinel peridotites reveal numerous, needle-shaped spinel crystals and inhomogeneously distributed spinel octahedra in olivine (Fig. 2). The most common are needles with a typical length of 5–25 µm and 50–200 nm width, which are concentrated in some areas of a grain, thus forming swarm-like pattern with the same crystallographic orientation. Other areas of the same grain may contain only a few needles or they are completely absent. The spinel needles often occur in the center of the grains and have no relation to microfractures in the olivine grains or trails of fluid inclusions. They are found in veined metasomatized samples as well as in ultramafic xenoliths without obvious metasomatic alteration. Two typical ultramafic xenoliths – one veined metasomatized lherzolite and one harzburgite without obvious secondary alterations – were selected and investigated with the microprobe and TEM.

Sample 56-2P is a granular spinel harzburgite with minor amounts of clinopyroxene. It mainly consists of olivine with $Fo_{90–91}$, which displays a bell-shaped zonation pattern with significantly decreasing Ca-content from core (120 ppm) to rim (1 ppm). Orthopyroxene with X_{Mg} [$=Mg/(Mg + Fe^{2+})$] -values of 0.9, contains low concentrations of Al_2O_3 (1.4 wt%) and Cr_2O_3 (0.3 wt%) and has a wollastonite component (Wo) of 0.9–1.2 mol%. Numerous exsolution lamellae of clinopyroxene are found in the orthopyroxene. Mapping of the orthopyroxene using a 50-µm beam of the microprobe leads to significantly higher concentrations of Al, Cr and Ca than spot analyses with a beam diameter of 1 µm (Table 1). Clinopyroxene is Cr-diopside with $Wo_{43–44}$, $En_{53–54}$ and Fs_3 (calculation after Lindsley 1983), which contains plenty of exsolution lamellae of orthopyroxene. Charge balance constraints point to minor amounts or to an absence of ferric iron in clinopyroxene. Large, intergranular spinel octahedra with diameters of 0.1–0.9 mm are Cr-rich with X_{Cr} [$=Cr/(Cr + Al)$] values of 0.49–0.53 and X_{Mg} values of 0.59–0.61 (Table 1). Towards the rim of the spinel, a decrease in chromium and ferric iron at the expense of aluminum is observed.

As evident from the zonation pattern in olivine as well as the exsolution lamellae in pyroxene, a distinct cooling occurred in the xenolith. Pyroxene thermometry using the T BKN calibration of Brey and Köhler (1990) yields temperatures of ~820 °C, using point analyses of the pyroxenes while integrated analyses (mapping of the crystals using a 50-µm beam diameter of the microprobe) reveal temperatures of ~880 °C. Similarly, the spinel–olivine Fe–Mg-exchange geothermometer of Ballhaus et al. (1991) yields temperatures of ~770 °C for the core and 700 °C for the rim section of the large

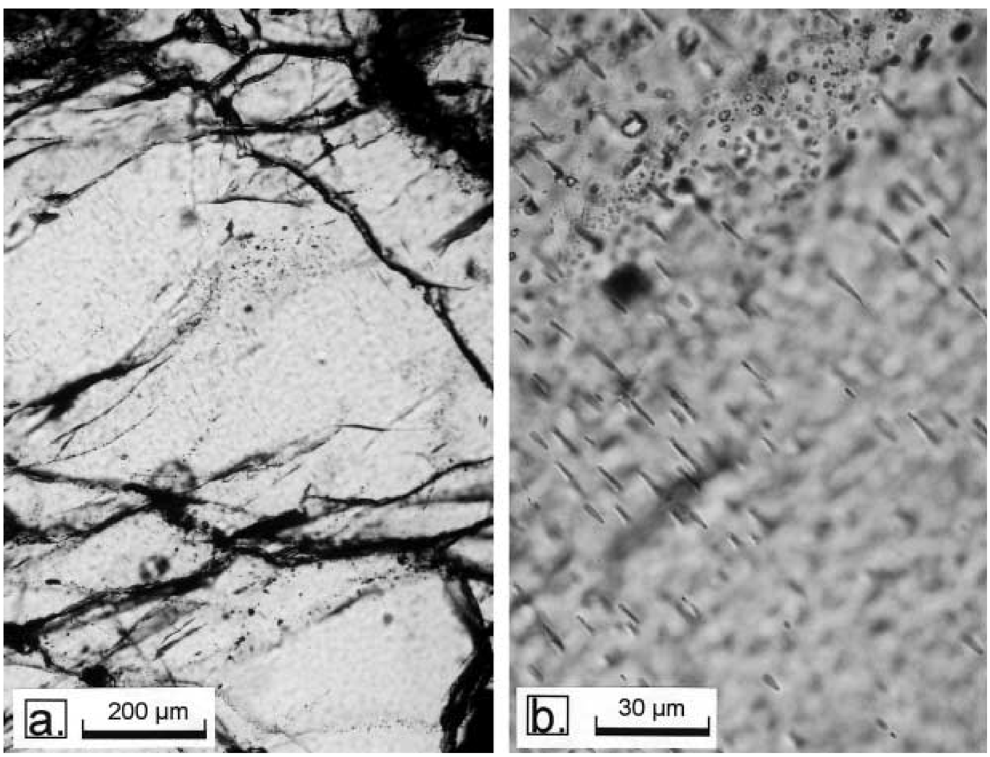

Fig. 2 **a** Microphotograph of an olivine grain with spinel needles Needles are accumulated in the central part of the grain and nearly absent at the rim (*upper left corner* and *right side* of the photograph). **b** Enlargement of **a** showing spinel needles near a trail of fluid inclusions. Note that there is no relation between the needles and the trail

Table 1 Representative analyses of spinel, olivine and pyroxene from sample 56-2P. Fe^{3+} estimated according to the method of Droop (1987). *AEM* analytical electron microscopy; *EMP* electron microprobe analysis; *n* number of analyses. T BBG and Delta log f_{O_2} are Ol–Spl thermometry and Ol–Spl–Opx oxygen barometry of Ballhaus et al. (1991)

Spl (wt%)	56-2P Al–Spl Core AEM	56-2P Lamella 1 AEM	56-2P Lamella 2 AEM	56-2P Lamella 3 AEM	56-2P Lamella 4 AEM	56-2P Lamella 5 AEM	56-2P Spl matrix Core EMP	56-2P Spl matrix Rim EMP	Ol (wt%)	56-2P Ol I avg. (n = 108) EMP	Cpx (wt%)	56-2P Cpx I Core EMP	Opx (wt%)	56-2P Opx I Core EMP
SiO_2	5.30	2.50	1.80	3.60	2.10	1.60	0.00	0.00	SiO_2	40.40	SiO_2	54.10	SiO_2	56.88
TiO_2	0.00	0.00	0.00	0.00	0.00	0.00	0.07	0.06	TiO_2	0.00	TiO_2	0.05	TiO_2	0.02
Al_2O_3	59.80	26.30	24.90	23.40	23.70	26.70	25.02	27.00	Al_2O_3	0.00	Al_2O_3	1.63	Al_2O_3	1.80
Cr_2O_3	0.20	40.30	40.40	38.70	41.10	37.60	41.43	39.86	Cr_2O_3	0.00	Cr_2O_3	0.73	Cr_2O_3	0.45
Fe_2O_3	0.00	0.00	3.30	3.72	3.18	5.29	2.91	2.70	MgO	50.42	Fe_2O_3	0.00	Fe_2O_3	0.00
MgO	25.20	14.50	16.10	17.90	15.90	17.20	12.32	12.71	CaO	0.01	MgO	17.46	MgO	33.35
CaO	0.00	0.00	0.00	0.00	0.00	0.00	0.00	0.01	MnO	0.00	CaO	23.60	CaO	0.71
MnO	0.00	0.00	0.00	0.00	0.00	0.00	0.13	0.12	FeO	8.65	MnO	0.06	MnO	0.17
FeO	9.50	16.30	13.73	13.16	14.24	12.14	16.33	16.01	NiO	0.38	FeO	1.72	FeO	5.67
ZnO	0.00	0.00	0.00	0.00	0.00	0.00	0.14	0.35	Total	99.86	Na_2O	0.09	Na_2O	0.00
NiO	0.00	0.00	0.00	0.00	0.00	0.00	0.10	0.08			K_2O	0.00	K_2O	0.01
Total	100.00	99.90	100.23	100.47	100.22	100.53	98.45	98.90			Total	99.44	Total	99.06
Cations (O = 4)									Cations (O = 4)		Cations (O = 6)		Cations (O = 6)	
Si	0.131	0.074	0.053	0.106	0.063	0.047	0.000	0.000	Si	0.988	Si	1.968	Si	1.974
Ti	0.000	0.000	0.000	0.000	0.000	0.000	0.002	0.001	Ti	0.000	Ti	0.001	Ti	0.001
Al	1.739	0.922	0.871	0.809	0.834	0.920	0.914	0.972	Al	0.000	Al	0.070	Al	0.074
Cr	0.004	0.947	0.948	0.898	0.970	0.869	1.015	0.963	Cr	0.000	Cr	0.021	Cr	0.012
Fe^{3+}	0.000	0.000	0.074	0.082	0.071	0.117	0.068	0.062	Mg	1.839	Fe^{3+}	0.000	Fe^{3+}	0.000
Mg	0.927	0.643	0.713	0.783	0.707	0.750	0.569	0.579	Ca	0.000	Mg	0.947	Mg	1.726
Ca	0.000	0.000	0.000	0.000	0.000	0.000	0.000	0.000	Mn	0.000	Ca	0.920	Ca	0.027
Mn	0.000	0.000	0.000	0.000	0.000	0.000	0.003	0.003	Fe	0.177	Mn	0.002	Mn	0.005
Fe^{2+}	0.196	0.405	0.341	0.323	0.355	0.297	0.423	0.409	Ni	0.007	Fe^{2+}	0.052	Fe^{2+}	0.165
Zn	0.000	0.000	0.000	0.000	0.000	0.000	0.003	0.008	Total	3.012	Na	0.006	Na	0.000
Ni	0.000	0.000	0.000	0.000	0.000	0.000	0.003	0.002	CaO (ppm)	131	K	0.000	K	0.001
Total	2.997	2.991	3.000	3.000	3.000	3.000	3.000	3.000	Cr_2O_3 (ppm)	15	Total	3.988	Total	3.983
									Al_2O_3 (ppm)	20				
X_{Mg}	0.83	0.61	0.68	0.71	0.67	0.72	0.57	0.58	End-members		End-members After Lindsley (1983)		End-members	
									Mg_2SiO_4	90.88				
X_{Cr}	0.00	0.51	0.52	0.53	0.54	0.49	0.53	0.50	Fe_2SiO_4	8.74			$Fe_2Si_2O_6$	8.57
P (kbar)	15.0	15.0	15.0	15.0	15.0	15.0	15.0	15.0	Ca_2SiO_4	0.02	Wo:	43.30	$Mg_2Si_2O_6$	89.79
T BBG	758	713	877	936	862	971	725	719	Ni_2SiO_4	0.37	En:	53.70	$Mn_2Si_2O_6$	0.26
Delta $logf_{O2}$	–	–	−0.18	0.00	−0.23	0.54	−0.22	−0.32	Mn_2SiO_4	0.00	Fs:	3.00	$Ca_2Si_2O_6$	1.38

spinel octahedra and adjacent olivine grains. A pressure estimate is rather problematic because of distinct mineral disequilibria caused by strongly different diffusion coefficients for the elements of concern in different minerals (cf. Franz et al. 2000). An intersection of the recent geothermal gradient of the Bismarck Archipelago with the K_D-line of the T BKN thermometry results in a pressure–temperature (P–T) estimate of 820 °C at 16.6 kbar.

Sample 56-2X is a coarse-equant spinel lherzolite, which is crosscut by a 5-mm-wide metasomatic vein consisting of phlogopite, hornblende, secondary clinopyroxene, garnet, anorthite, and mackinawite. An explicit description of the mineral chemistry and the metasomatic reactions, which generated this vein, is presented elsewhere (Franz et al. 2000). The primary mineral assemblage mainly consists of coarse-grained olivine (Fo_{91-92}), which again shows the typical, retrograde zoning of Ca (100 ppm Ca in the core vs 34 ppm Ca in the rim). Ortho- and clinopyroxene do not show exsolutions under the petrographic microscope but display distinct chemical zoning. Orthopyroxene (X_{Mg}0.91–0.92) shows a decrease of the wollastonite component from core to rim (1.2 mol% vs. 0.47 mol% Wo) as well as decreasing Al and Cr concentration in the same direction. Clinopyroxene displays a composition of $Wo_{46}En_{52}Fs_2$ in the core and $Wo_{43}En_{54}Fs_3$ in the rim section. These features again testify to distinct cooling processes in the mantle. Intergranular spinel octahedra display typical zonation patterns with abruptly decreasing Cr and Al contents at the expense of Fe^{3+}, which is especially prominent near the metasomatic vein. Spinel needles are present in some of the large olivine grains remote from the metasomatic vein. Selected mineral analyses are presented in Tables 2 and 3 as well as in Franz et al. (2000).

Thermobarometry applied to core analyses of pyroxenes yields a temperature of ~930 °C (at 10 kbar) using the T BKN calibration, whereas analyses from the corresponding rim sections indicate cooling processes (720 °C at 10 kbar). Temperatures calculated with the olivine–spinel geothermometer of Ballhaus et al. (1991) are in the range of 750 °C for the core sections of the minerals, whereas analyses from the rim sections yield 720–740 °C. The P–T estimate for the metasomatic overprint is 720–770 °C at 4–8 kbar (Franz et al. 2000). Quite remarkable is the elevated oxygen fugacity ($\Delta\log f_{O_2} = 1.3$ to 2.5; cf. Franz et al. 2000) during the metasomatic overprint, which is a typical feature of the metasomatic peridotites of this region resulting from he hydrous fluids generated by dehydration of the underlying subducted slab (see also McInnes et al. 2000).

Inclusions in olivine

Both samples reveal numerous inclusions in olivine, which commonly have sizes of less than a micron. TEM investigations show that the majority of these inclusions are different types of spinel.

1. The most common are spinel needles, which display a crystallographic orientation in the olivine grains. The orientation relationship is given by: $[001]_{Ol}//[1\bar{1}0]_{Spl}$ and $(100)_{Ol}//(111)_{Spl}$ (see Fig. 3). The needles are elongated in a parallel [010] direction in olivine and oriented parallel to the (111) plane of spinel. The precipitates are semi-coherent because only the d-spacings of the parallel planes $(100)_{Ol}$ ($d = 0.4762$ nm) and $(111)_{Spl}$ ($d = 0.481$ nm) have a similar lattice spacing. The needles have a typical length of 8 μm (see Fig. 2) although some olivine grains bear irregularly shaped spinel needles with serrated rims and a length exceeding 25 μm. TEM investigations reveal a lenticular shape of the needles with widths and depths of 50–200 nm. Because of their small size, the composition of the spinel needles can only be determined by AEM. In sample 56-2P, spinel needles yield rather uniform compositions with X_{Mg} values of 0.61–0.72 and X_{Cr} values of 0.49–0.55, thus resembling the intergranular spinel octahedra (Table 1). Differences in X_{Mg} arise from secondary fluorescence effects of the hosting olivine leading to elevated SiO_2 and consequently increased MgO-concentrations because the chemical composition is normalized to 100%. Consequently, because of these analytical limitations, an estimate of the Fe^{3+}-content of the spinel needle is affected by an error.

2. In sample 56-2X, spinel needles show a wide variability in composition ranging from specimens with intermediate Cr and Al contents (~39 wt% Cr_2O_3 and 21 wt% Al_2O_3) to Cr-rich types (48.5–55.8 wt% Cr_2O_3 and 7.2–16.4 wt% Al_2O_3). As evident from the chemical analyses (Table 2 and Fig. 7), the spinel needles with intermediate Cr- and Al-concentrations resemble the intergranular spinel octahedra.

3. Small spinel octahedra included in olivine with typical diameters of 200–400 nm occur in both samples and reveal the same orientation relationship with respect to olivine as the spinel needles (Fig. 4). They are distinguished from the spinel needles by their different chemical composition with an extreme enrichment in Al (41.2–59.8 wt% Al_2O_3) and low Cr concentrations (2.0–5.3 wt% Cr_2O_3; Tables 1 and 2). As evident from the SiO_2 contents of these grains, which are in the range of 2.2 and 5.3 wt%, a secondary fluorescence of the hosting olivine cannot be excluded.

4. Tiny idiomorphic magnetite grains, which appear in sample 56-2X, show diameters of ~200 nm and exhibit the same orientation relationship with the host olivine as that of spinel needles: $[001]_{Ol}//[1\bar{1}0]_{Spl}$ and $(100)_{Ol}//(111)_{Spl}$ (Fig. 5). This orientation relationship was earlier reported for magnetite inclusions in olivine by Champness (1970). The magnetite grains have a certain amount of Cr and Mg (Table 2) and are often associated with cavities. In one case NaCl was found in such a cavity together with orthopyroxene. The same mineral paragenesis of magnetite, orthopyroxene and NaCl in olivine was described by Puga et al. (1999).

Table 2 Representative analyses of spinel from sample 56-2X. Fe^{3+} estimated according to the method of Droop (1987). *AEM* analytical electron microscopy; *EMP* electron microprobe analysis; *n* number of analyses. T BBG and Delta log f_{O_2} are Ol–Spl thermometry and Ol–Spl–Opx oxygen barometry of Ballhaus et al. (1991)

Spl (wt%)	56-2X Al-Spl Core AEM	56-2X Al-Spl Core AEM	56-2X Magnetite Core AEM	56-2X Lamella 1 AEM	56-2X Lamella 2 AEM	56-2X Lamella 3 AEM	56-2X Lamella 4 AEM	56-2X Lamella 5 AEM	56-2X Spl matrix Rim AEM	56-2X Spl Matrix Rim AEM	56-2X Spl matrix Rim AEM	56-2X Spl matrix Rim AEM	56-2X Spl matrix Core EMP	56-2X Spl matrix Rim EMP
SiO_2	2.20	4.30	2.45	2.00	1.10	1.50	2.00	1.40	0.40	0.90	0.40	0.50	0.14	0.48
TiO_2	0.00	0.00	1.51	0.00	0.00	0.80	0.00	0.00	0.00	0.00	0.00	0.00	0.15	0.63
Al_2O_3	54.50	41.20	5.38	12.80	5.90	5.40	12.80	22.10	21.60	18.50	18.90	19.80	27.99	20.80
Cr_2O_3	2.00	4.10	3.11	46.70	59.10	57.80	46.70	42.90	42.90	39.50	51.20	49.50	40.46	36.69
Fe_2O_3	7.96	16.32	56.85	9.07	5.88	4.75	9.07	4.32	5.55	11.84	0.00	0.00	0.64	10.52
MgO	18.60	15.40	11.13	12.30	11.20	10.30	12.30	14.60	12.20	12.20	9.70	10.00	12.32	11.66
CaO	0.00	3.30	0.00	0.00	0.00	0.00	0.00	0.00	0.00	0.00	0.00	0.00	0.00	0.01
MnO	0.00	0.00	0.00	0.00	0.00	0.00	0.00	0.00	0.00	0.00	0.00	0.00	0.00	0.00
FeO	15.03	16.91	19.58	18.03	17.41	19.93	18.03	15.12	17.20	17.44	19.70	20.10	17.63	17.87
ZnO	0.00	0.00	0.00	0.00	0.00	0.00	0.00	0.00	0.00	0.00	0.00	0.00	0.06	0.14
NiO	0.00	0.00	0.00	0.00	0.00	0.00	0.00	0.00	0.00	0.00	0.00	0.00	0.09	0.25
Total	100.30	101.53	100.00	100.90	100.59	100.47	100.91	100.43	99.85	100.38	99.90	99.90	99.49	99.04
Cations (O = 4)														
Si	0.058	0.118	0.083	0.064	0.036	0.050	0.064	0.042	0.012	0.028	0.013	0.016	0.004	0.015
Ti	0.000	0.000	0.039	0.000	0.000	0.020	0.000	0.000	0.000	0.000	0.000	0.000	0.003	0.015
Al	1.686	1.336	0.216	0.480	0.231	0.213	0.480	0.789	0.791	0.684	0.708	0.738	1.000	0.774
Cr	0.042	0.089	0.084	1.175	1.550	1.527	1.175	1.028	1.054	0.980	1.286	1.238	0.970	0.916
Fe^{3+}	0.157	0.338	1.456	0.217	0.147	0.119	0.217	0.098	0.130	0.280	0.000	0.000	0.015	0.250
Mg	0.728	0.632	0.565	0.584	0.554	0.513	0.584	0.659	0.565	0.571	0.460	0.472	0.557	0.549
Ca	0.000	0.097	0.000	0.000	0.000	0.000	0.000	0.000	0.000	0.000	0.000	0.000	0.000	0.000
Mn	0.000	0.000	0.000	0.000	0.000	0.000	0.000	0.000	0.000	0.000	0.000	0.000	0.000	0.000
Fe^{2+}	0.330	0.389	0.557	0.480	0.483	0.557	0.480	0.383	0.447	0.458	0.524	0.532	0.447	0.472
Zn	0.000	0.000	0.000	0.000	0.000	0.000	0.000	0.000	0.000	0.000	0.000	0.000	0.001	0.003
Ni	0.000	0.000	0.000	0.000	0.000	0.000	0.000	0.000	0.000	0.000	0.000	0.000	0.002	0.006
Total	3.000	3.000	3.000	3.000	3.000	3.000	3.000	3.000	3.000	3.000	2.990	2.996	3.000	3.000
X_{Mg}	0.69	0.62	0.50	0.55	0.53	0.48	0.55	0.63	0.56	0.55	0.47	0.47	0.55	0.54
X_{Cr}	0.02	0.06	0.28	0.71	0.87	0.88	0.71	0.57	0.57	0.59	0.65	0.63	0.492	0.54
P(kbar)	10.0	10.0	10.0	10.0	10.0	10.0	10.0	10.0	10.0	10.0	10.0	10.0	10.0	10.0
T BBG	476	523	1001	753	823	755	754	752	680	729	595	583	590	687
Delta log f_{O_2}	3.72	4.48	5.69	2.21	1.41	1.17	2.21	0.88	1.43	2.71	–	–	−2.10	2.64

Table 3 Representative analyses of olivine, pyroxene, melt inclusions, and a cavity filling from sample 56-2X. Fe^{3+} estimated according to the method of Droop (1987). *AEM* analytical electron microscopy; *EMP* electron microprobe analysis; *n* number of analyses. T BBG and Delta log f_{O_2} are Ol–Spl thermometry and Ol–Spl–Opx oxygen barometry of Ballhaus et al. (1991)

Ol (wt%)	56-2X Ol 1 avg. ($n = 93$) EMP	Cpx (wt%)	56-2X Cpx I Core EMP	Opx (wt%)	56-2X Opx I Core EMP	56-2X Opx II Core AEM	Melt inclusions in olivine (wt%)	56-2X Melt Gl Core AEM	56-2X Melt G4 Core AEM	56-2X Melt G5 Core AEM	56-2X Melt A3 Core AEM	Cavity filling: NaCl+Ol+Opx (wt%)	56-2X Center AEM
SiO_2	40.16	SiO_2	54.23	SiO_2	57.55	55.55	SiO_2	42.90	47.10	28.20	40.80	SiO_2	47.90
TiO_2	0.00	TiO_2	0.23	TiO_2	0.09	0.00	Al_2O_3	1.90	1.60	1.90	1.70	Al_2O_3	0.00
Al_2O_3	0.00	Al_2O_3	2.15	Al_2O_3	1.46	0.00	Cr_2O_3	2.60	1.60	3.50	4.50	Cr_2O_3	0.00
Cr_2O_3	0.00	Cr_2O_3	0.90	Cr_2O_3	0.34	0.00	MgO	35.40	30.60	26.00	30.60	MgO	32.20
MgO	50.88	Fe_2O_3	0.00	Fe_2O_3	0.00	8.00	CaO	0.90	1.70	0.80	3.10	CaO	0.00
CaO	0.02	MgO	17.64	MgO	35.27	37.30	FeO	13.10	14.30	34.30	15.50	FeO	6.20
MnO	0.00	CaO	22.98	CaO	0.63	0.00	NiO	1.80	1.80	2.30	1.30	Na_2O	3.10
FeO	7.10	MnO	0.07	MnO	0.14	0.00	Na_2O	0.00	0.00	0.00	0.00	K_2O	0.00
NiO	0.34	FeO	1.79	FeO	5.20	0.00	K_2O	1.30	1.30	2.40	2.60	Cl_2O	10.70
Total	98.51	Na_2O	0.36	Na_2O	0.00	0.00	Total	99.90	100.00	99.40	100.10	Total	100.10
Cations (O = 4)		K_2O	0.02	K_2O	0.00	0.00	Ol-melt Fe–Mg exchange thermometry after Ford et al. (1983)						
Si	0.989	Total	100.38	Total	100.67	100.85	P (kbar)	10.0	10.0	10.0	10.0		
Ti	0.000	Cations (O = 6)		Cations (O = 6)			T_{Mg} (°C)	1092	1296	1235	1205		
Al	0.000	Si	1.954	Si	1.963	1.897	T_{Fe} (°C)	942	1189	1699	1149		
Cr	0.000	Ti	0.006	Ti	0.002	0.000							
Mg	1.868	Al	0.091	Al	0.059	0.000							
Ca	0.001	Fe^{3+}	0.000	Fe^{3+}	0.000	0.206							
Mn	0.000	Cr	0.026	Cr	0.009	0.000							
Fe	0.146	Mg	0.948	Mg	1.793	1.898							
Ni	0.007	Ca	0.887	Ca	0.023	0.000							
Total	3.011	Mn	0.002	Mn	0.004	0.000							
CaO (ppm)	225	Fe^{2+}	0.054	Fe^{2+}	0.148	0.000							
Cr_2O_3 (ppm)	20	Na	0.025	Na	0.000	0.000							
Al_2O_3 (ppm)	20	K	0.001	K	0.000	0.000							
	92.40	Total	3.994	Total	4.001	4.001							
End-members		End-members after Lindsley (1983)		End-members									
Mg_2SiO_4													
Fe_2SiO_4	7.24			$Fe_2Si_2O_6$	7.53	0.00							
Ca_2SiO_4	0.03	Wo	42.10	$Mg_2Si_2O_6$	91.10	100.00							
Ni_2SiO_4	0.34	En	54.80	$Mn_2Si_2O_6$	0.20	0.00							
Mn_2SiO_4	0.00	Fs	3.10	$Ca_2Si_2O_6$	1.17	0.00							

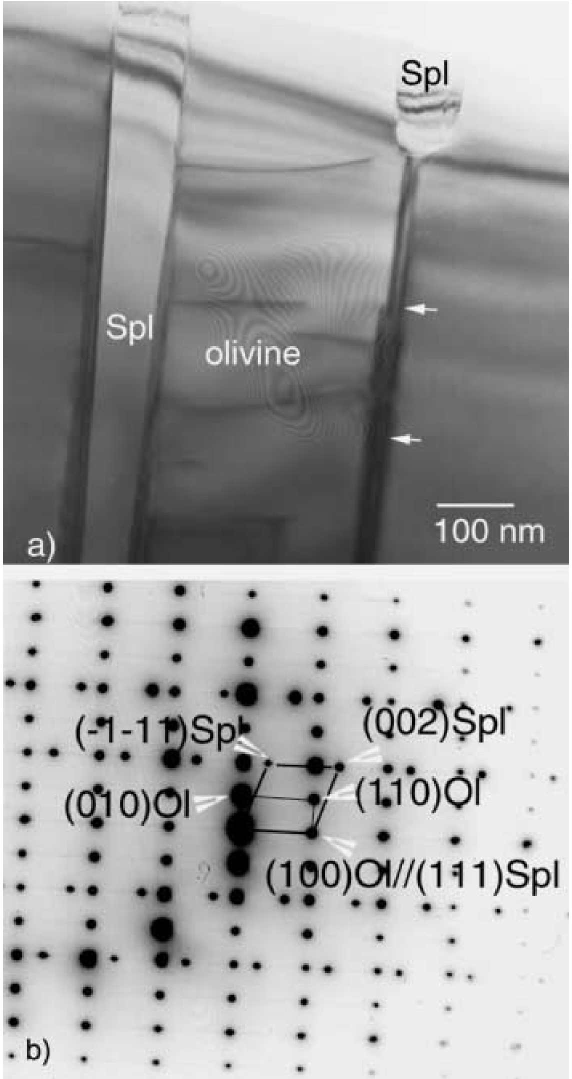

Fig. 3 **a** TEM bright-field image showing two spinel needles in olivine (sample 56-2X). Note that the spinel needles run parallel to the low-angle grain boundary in olivine. The interface is oriented parallel to the beam, therefore no dislocation lines are visible. **b** Corresponding $[001]_{Ol}$ diffraction pattern revealing the orientation relationship between spinel and olivine $(100)_{Ol}//(111)_{Spl}$, and $[001]_{Ol}//[1\bar{1}0]_{Spl}$

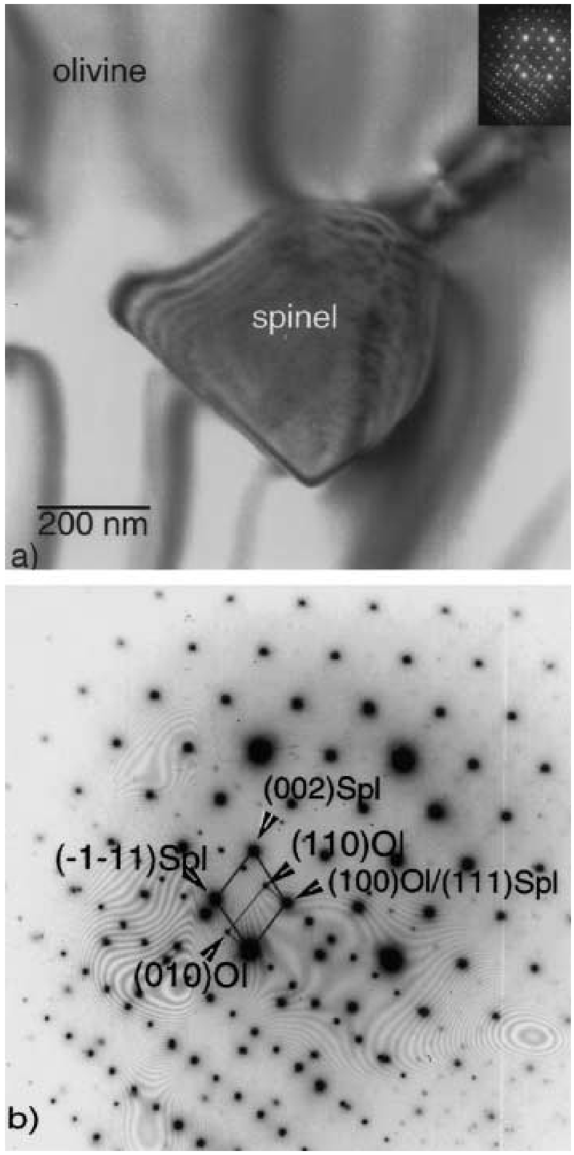

Fig. 4 **a** TEM bright field image showing an Al-spinel octahedron in olivine of sample 56-2P with diffraction pattern inserted **b** $[001]_{Ol}$ diffraction pattern revealing the orientation relationship between spinel and olivine

The secondary orthopyroxene in sample 56-2X reveals a rather peculiar composition with Ca, Na and Al contents below the detection limit of the AEM, and charge balance constraints point to a mere presence of ferric iron (cf. Table 3). The analysis of NaCl from the cavity is characterized by strong secondary fluorescence and/or influence of the underlying olivine grain (Table 3).

Beside orthopyroxene and NaCl, cavities in olivine often contain idiomorphic calcite and $CaCl_2$. Furthermore, fluid inclusions are present along healed cracks linked with dislocations. The olivine crystals show a remarkable microstructure. They exhibit long, straight dislocation lines, which indicates deformation by dislocation glide. Nearly all of the olivine grains are subdivided into subgrains by parallel low-angle grain boundaries (Fig. 6). The subgrains have a typical width of ~1 μm. Very often, fluid inclusion bubbles or melt inclusions are associated with the low-angle grain boundaries. The melt inclusions have an ultramafic composition with variable concentrations of SiO_2 (28–47 wt%; Table 3). According to the Fe–Mg-exchange geothermometer of Ford et al. (1983), temperatures of ~1100–1300 °C (TMg, Table 3) were calculated for these melt inclusions and the surrounding olivine, which points to the generation of that melt by the host basalt. Healed cracks are decorated with fluid inclusion bubbles. Furthermore, the spinel/olivine interface shows numerous fluid inclusion bubbles, which are commonly linked with dislocations.

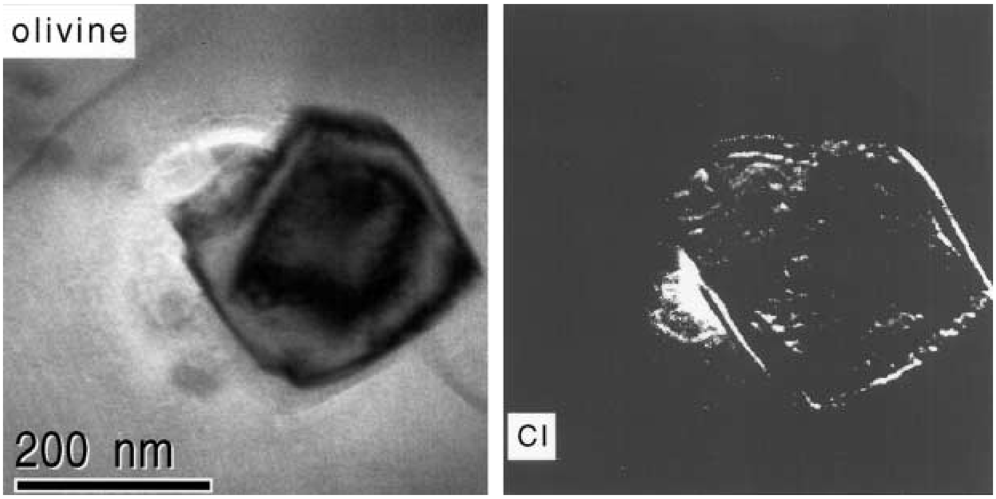

Fig. 5 Elemental map of a magnetite inclusion in olivine of sample 56-2X using Cl. In the *upper left corner* is the corresponding energy-filtered bright field image (zero-loss filtering, energy window 10 eV). Note the chlorine in the cavity, which stems from NaCl

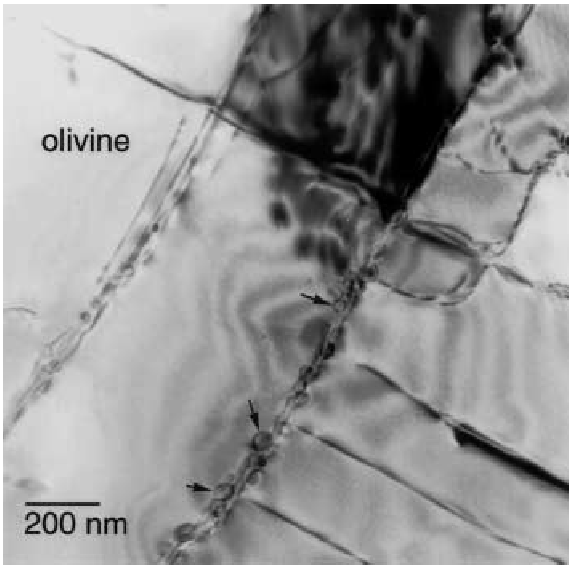

Fig. 6 TEM dark-field image of two parallel low-angle grain boundaries in olivine. Note the tiny fluid inclusion bubbles decorating the low-angle grain boundary

Discussion

The literature contains several models that explain the formation of spinel needles and symplectites. The following section gives an evaluation of these models with respect to the formation of the observed spinel inclusions in the xenoliths of TUBAF seamount.

1. Breakdown of garnet inclusions in olivine, as postulated by Bell et al. (1975), cannot explain the formation of any spinel inclusions in olivine. Such a breakdown usually generates symplectites of olivine, spinel as well as ortho- and clinopyroxene, which were not observed within olivine in the TUBAF xenoliths.

2. Breakdown of phlogopite might be responsible for the formation of the aluminous spinel octahedra in both investigated samples. According to Pasteris (1983), the reaction

$$\underset{\text{phlogopite}}{4KMg_3[(OH)_2AlSi_3O_{10}]} \Longleftrightarrow \underset{\text{forsterite}}{5Mg_2[SiO_4]} + \underset{\text{spinel}}{2MgAl_2O_4} + \underset{\text{melt}}{(2K_2O + 4H_2O + 7SiO_2)}$$

which he observed in the DeBeers kimberlite, may lead to the generation of spinel similar in composition to the aluminous spinel octahedra in the TUBAF samples. The exact time of this event, however, cannot be determined. Phlogopite breakdown could have occurred during the plume-induced heating of the asthenosphere, during the initial formation of the mid-ocean ridge or during the influence of fluids emerging from the Quaternary host basalt. As the minimum temperatures for the breakdown of phlogopite are ~850 °C (Wagner and Velde 1987) the metasomatism by the slab-derived aqueous fluids can surely be excluded for the formation of the aluminous spinel. Another possibility is the influence of metasomatic fluids, which may have produced this spinel by complex cation exchanges. Metasomatic aluminous spinel with a similar composition was described in kimberlites by Haggerty (1988; Fig. 7).

3. Oxidation and cellular decomposition (Putnis 1979) can be rejected for the generation of the chromian and the aluminous spinel because the shape of the inclusions does not resemble at all the products of such a process (see Putnis 1979; Moseley 1984) and furthermore, neither the composition of these spinel inclusions (which should be magnetite in case of the oxidation) nor accompanying pyroxene was observed in the TUBAF xenoliths. However, the few magnetite grains may well be generated by such an oxidation. The finding of excavations with NaCl phase near the magnetite and the presence of associated orthopyroxene points to a reaction:

$$\underset{\text{olivine}}{6(Fe,Mg)_2[SiO_4]} + \underset{\text{oxygen}}{O_2} \Longleftrightarrow \underset{\text{magnetite}}{2Fe_3O_4} + \underset{\text{enstatite}}{3Mg_2[Si_2O_6]}$$

with a hydrous, saline fluid phase acting as the oxidizing agent (for the reaction mechanism see Champness 1970). Puga et al. (1999) describe magnetite inclusions in olivine from ophiolitic metagabbros associated with

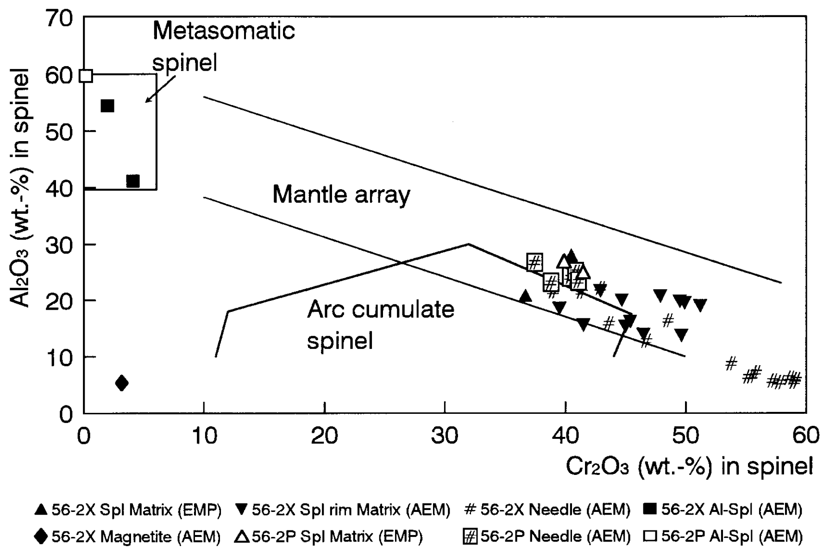

Fig. 7 Al_2O_3 vs Cr_2O_3 diagram for spinel of samples 56-2P and 56-2X. Fields of arc cumulate spinel, metasomatic spinel and mantle array after Conrad and Kay (1984), Haggerty (1988), and Kepezhinskas et al. (1995)

orthopyroxene and NaCl. There, NaCl is indicative for seawater influence on the formation of magnetite in olivine. A coupled exsolution process of fluid and spinel in olivine as proposed by Green (1985; see also Burns 1975) seems rather improbable for the TUBAF xenoliths. According to these authors, the existence of dissolved carbon and O^- in olivine may lead to the formation of spinel inclusions during decompression. However, such a mechanism would always be connected with the formation of syngenetic CO_2 fluid inclusions and in part with the generation of native carbon, which both have not been observed near the magnetite octahedra nor the other spinel inclusions in olivine of the TUBAF xenoliths.

5. Another possibility to explain the presence of magnetite inclusions in olivine would be the decomposition of high-P, Fe^{3+}-bearing olivine as observed by Zhang et al. (1981, 1999) in ultrahigh-pressure rocks. For the TUBAF xenoliths, this mechanism seems improbable as there are no indications of any high-pressure event. The same applies to the generation of spinel needles by exsolution of wadsleyite solid solution during decompression (Zhang et al. 1999).

6. The generation of chromian spinel inclusions in olivine was investigated by Duke (1976), who found that olivine crystallizing from a chromium rich melt may incorporate elevated amounts of Cr^{3+}. During subsequent annealing chromian spinel may exsolve (Arai 1978). However, this model cannot be applied to the TUBAF xenoliths because they are not magmatic cumulates, but represent depleted lithospheric mantle, which equilibrated in the stability field of spinel peridotite. For the same reason, a simultaneous crystallization of chromian spinel and olivine from a mafic parental magma can be excluded.

7. A process that may lead to the generation of chromian spinel inclusions in olivine could result from cooling and decompression of Cr- and Al-rich olivine in the mantle under the mid-ocean ridge. At high temperature and pressure, olivine may incorporate elevated amounts of Cr and Al, as shown by Dodd (1973) for olivine of the Sharps chondrite. Based on analytical data, Dodd (1973) proposed a coupled substitution of Al + Cr^{3+} <=> Si^{4+} + (Mg,Fe^{2+}) in olivine. On cooling, unmixing processes could have led to the formation of the Cr- and Al-rich spinel needles found in the olivine of the TUBAF xenoliths via the reaction:

$$\underset{\text{Cr-, Al-rich olivine}}{(Mg,Fe^{2+})_{2-x}Cr_x[Al_xSi_{1-x}O_4]} \Longleftrightarrow \underset{\text{Cr-Al-spinel}}{x(Mg,Fe^{2+})CrAlO_4} + \underset{\text{olivine}}{1-x(Mg,Fe^{2+})_2[SiO_4]}$$

This mechanism explains the presence of single phase spinel inclusions as well as their specific chemical composition. A quantification of the solubility of Al and Cr in olivine at elevated pressures and temperatures has been undertaken by Köhler (1989), who showed that olivine may incorporate up to 710 ppm Cr_2O_3 and 450 ppm Al_2O_3 at 1200 °C and 20 kbar. These P–T values would be similar to the conditions in the upper oceanic asthenosphere during the formation of the basaltic magma in the course of mid-ocean ridge spreading. On cooling and decompression, solubility for Al and Cr is decreasing (see Köhler 1989), which may have given way to the exsolution of the spinel needles.

The question is whether these low contents of Cr and Al in olivine were really sufficient to produce the observed spinel needles by exsolution. For this reason, the Al- and Cr-contents of selected olivine grains were determined by microprobe analyses with elevated beam current acceleration voltages and counting times (see above) along traverses through selected olivine grains. For the olivine of sample 56-P, an average content of 15 ppm for Cr_2O_3 and of 20 ppm for Al_2O_3 were measured and similarly low contents of 20 ppm for Cr_2O_3 and Al_2O_3 were detected in olivine of sample 56-2X (see Tables 1 and 3). This is close to the detection limit of the probe and shows that olivine from both samples was almost devoid of these elements. To determine the amount of Cr and Al in the spinel needles, all needles from an inclusion-rich olivine grain from sample 56-2P were counted and their lengths were measured under the optical microscope. The procedure revealed a number of 1415 needles with an average length of ~8 μm. As indicated by the TEM studies, the needle-shaped spinel crystals have a maximum width and depth of 200 nm. Using these data, the total volume of all needles was calculated. Because of their tiny width and depth, the spinel needles occupied a volume of only 0.0013% in the hosting olivine. Even in sections of the olivine grains with an accumulation of spinel inclusions, their volume did not exceed 0.0044%. As evident from the AEM analyses, a typical chromian spinel needle yields an average of 25 wt% Al_2O_3 and 40% wt% Cr_2O_3, and thus, all observed needles cause an increase of about 3 ppm Al_2O_3 and 5 ppm Cr_2O_3 in the hosting olivine grain. Even in sections with an accumulation of spinel inclusions, the increase does not exceed 11 ppm Al_2O_3 and 18 ppm Cr_2O_3 and therefore, these needles may well have formed by exsolution. Any additional amount of Cr and Al contained in the high-temperature olivine could have left the grain by diffusion during cooling forming the large, intergranular spinel octahedra.

These interpretations are supported by the Al_2O_3 vs Cr_2O_3 diagram for spinel (Fig. 7), which reveals the variability in composition of the different spinel types and shows that all chromian spinel (i.e. intergranular spinel and spinel needles) plot in the mantle array outlined by Kepezhinskas et al. (1995). In contrast to this, aluminous spinel plots in the field of metasomatic spinel, which, however, also includes spinel generated by breakdown of aluminous silicates (see Wagner and Velde 1987; Haggerty 1988; Mukhopadhyay 1991).

Conclusion

The presence of numerous spinel inclusions in olivine from mantle xenoliths of the TUBAF seamount can be assigned to genetically different processes. Magnetite octahedra, which are usually accompanied by orthopyroxene and formerly fluid-filled cavities are supposed to have formed by oxidation of the olivine grain. The oxidizing agent may have been generated by dehydration of the underlying, subducted Pacific plate or may be derived from the volatile rich, Quaternary volcanism (McInnes et al. 2000), which transported the xenoliths to the surface.

Rare aluminous spinel octahedra are probably the breakdown product of an Al-rich phase such as phlogopite or may also have developed under the influence of a metasomatic fluid. However, because of missing textural relationships and the absence of accompanying critical phases, the time of their generation cannot be determined.

The majority of the spinel inclusions, consisting of chromian spinel needles, are assumed to have formed by exsolution processes. The mantle peridotite xenoliths from TUBAF seamount in the Bismarck Archipelago of Papua New Guinea give evidence for distinct cooling processes, which are interpreted to have taken place during the formation of the mantle lithosphere under the mid-ocean ridge (Franz et al. 2000). The formation of lithospheric mantle is well described by models of Houseman and McKenzie (1982), Houseman (1983a, b), or Rabinowicz et al. (1984), who postulate a rolling mill effect of the mantle at mid-ocean ridges. According to these authors partial melting and melt extraction processes affect the ultramafics during their uplift, thus creating the depleted lithospheric mantle. As evident from investigations of meteorites (Dodd 1973) and from experiments of Köhler (1989), olivine may incorporate elevated concentrations of Cr and Al at higher temperatures. During uprise from the hot asthenosphere, olivine must have exsolved the observed Cr- and Al-rich spinel needles. An argument for such exsolution processes is the crystallographic orientation of the needles in the olivine grains. Volumetric calculations have shown, that the amount of Cr and Al of high-temperature olivine is sufficient to have produced these spinel exsolutions. During the thermal equilibration in the upper mantle lithosphere, the spinel needles, as well as the large intergranular spinel octahedra, experienced a resetting of their chemistry, which is visible in sample 56-2P. Spinel needles reveal a very similar composition to the intergranular spinel specimen and deviations mainly result from analytical inaccuracy (i.e. incorporation of the hosting olivine in the analysis). Because of this analytical error, a calculation of Fe–Mg-exchange thermometry between the spinel needles and the olivine results in a wide scatter of the temperatures (i.e. 713–971 °C; see Table 1).

Although spinel needles in sample 56-2P reveal about the same X_{Cr}-values as the large intergranular octahedra, needles in sample 56-2X in part show significantly higher X_{Cr}-values than the large grains in the matrix (Fig. 8a, b). This variability in X_{Cr} can probably be ascribed to the metasomatism of fluids generated by dehydration of the underlying slab, which also caused the veining of this sample. Similar patterns of Cr-enrichment are revealed by microprobe analyses from the rim sections of intergranular spinel octahedra, which is especially prominent near the metasomatic vein of this sample (Fig. 8b). Compared with the Cr-rich needles, X_{Cr} of the intergranular octahedra still may seem rather low, but this is just a question of the analytical resolution. The microprobe beam never reaches the outermost rim section of the grain and only the use of AEM gives an insight into these domains. According to these AEM analyses, the composition of the outermost rim of the intergranular octahedra shows great resemblances to the composition of the tiny spinel needles, which highlights late processes of equilibration (see Table 2). Despite the analytical error of the AEM and despite the chemical re-equilibration of the spinel needles, most Fe–Mg-exchange temperatures with the hosting olivine are in the range of 700–800 °C

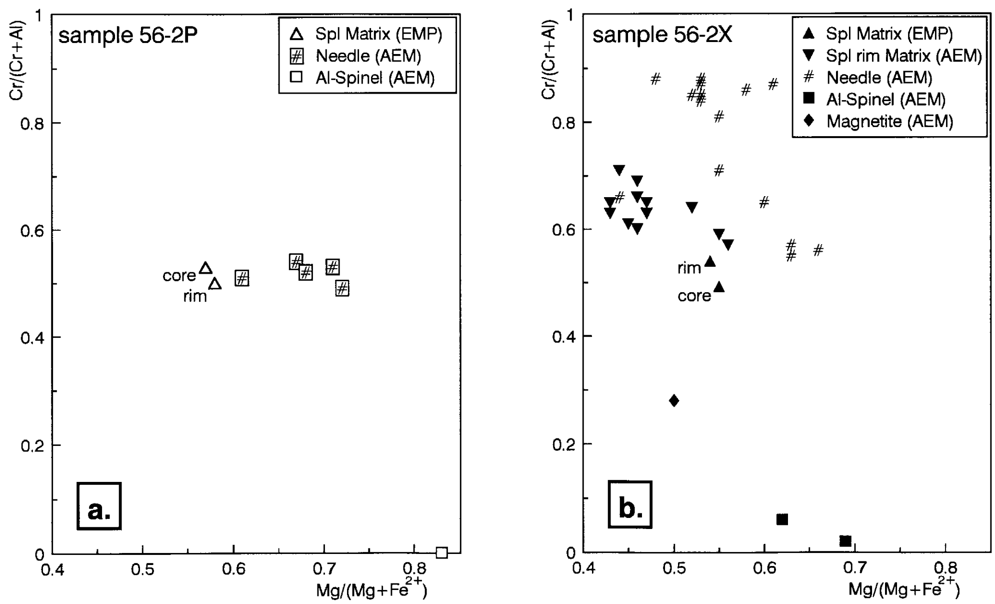

Fig. 8a, b X_{Cr} vs X_{Mg} diagrams for spinel of samples **a** 56-2P and **b** 56-2X

(see Table 2), thus corresponding to the temperatures estimated for the metasomatic event (see above and Franz et al. 2000). Furthermore, an elevated oxygen fugacity is revealed by these spinel needles applying the barometry of Ballhaus et al. (1991), which is also indicative of the metasomatism (see Table 2 and cf. Franz et al. 2000; McInnes et al. 2000).

These observations show that the formation of spinel inclusions and their compositional modification may be caused by different processes, which can eventually be observed in the same sample. Furthermore, it becomes evident that a knowledge of the geological setting and the physico-chemical processes affecting the rocks can be the key for the understanding of all the petrological observations.

Acknowledgements The authors thank Karin Paech (Potsdam) for her extraordinary skill in TEM specimen preparation and Klaus-Peter Becker (Freiberg) for the assistance with the microprobe. The manuscript was considerably improved by the inspiring reviews of Pamela Champness and Wolfgang Müller. We also want to thank Gerhard Brey and Thomas Stachel (Frankfurt) for helpful remarks and fruitful discussion. We owe great thanks for the logistic and scientific support to the master, officers and crew of research vessel RV *Sonne* during our research activities in the New Ireland basin. Special thanks are due to Peter Herzig (Freiberg), chief scientist of the research campaign, who enabled L.F. to participate in the Edison II cruise. Principal funding for this project was provided by the German Federal Ministry for Education and Science (BMBF Grant 03G0133A to Peter Herzig).

References

Arai S (1978) Chromian spinel lamellae in olivine from the Iwanai-Dake peridotite mass, Hokkaido, Japan. Earth Planet Sci Lett 39: 267–273

Ashworth JR (1979) Two kinds of exsolution in chondritic olivine. Mineral Mag 43: 535–538

Ballhaus C, Berry RF, Green DH (1991) High pressure experimental calibration of the olivine–orthopyroxene–spinel oxygen geobarometer: implications for the oxidation state of the upper mantle. Contrib Mineral Petrol 107: 27–40

Bell PM, Mao HK, Roedder E, Weiblen PW (1975) The problem of the origin of symplectites in olivine-bearing lunar rocks. Proc Sixth Lunar Sci Conf 1: 231–248

Brey GP, Köhler T (1990) Geothermobarometry in four-phase lherzolites II. New thermobarometers, and practical assessment of existing thermobarometers. J Petrol 31: 1353–1378

Burns RG (1975) Crystal field effects in chromium and its partitioning in the mantle. Geochim Cosmochim Acta 39: 857–864

Champness PE (1970) Nucleation and growth of iron oxides in olivines, $(Mg,Fe)_2SiO_4$. Mineral Mag 37: 790–800

Coleman PJ, Kroenke LW (1981) Subduction without volcanism in the Solomon Island arc. Geo-Mar Lett 1: 129–134

Conrad WK, Kay RW (1984) Ultramafic and mafic inclusions from Adak Island: crystallisation history, and implications for the nature of primary magmas and crustal evolution in the Aleutian arc. J Petrol 25: 88–125

Dodd RT (1973) Minor element abundances in olivines of the Sharps (H3) chondrite. Contrib Mineral Petrol 42: 156–167

Droop GTR (1987) A general equation for estimating Fe^{3+} concentrations in ferromagnesian silicates and oxides from microprobe analyses, using stoichiometric criteria. Mineral Mag 5: 431–435

Duke JM (1976) Distribution of the period four transition elements among olivine, calcic clinopyroxene and mafic silicate liquid: experimental results. J Petrol 17: 499–521

Egerton RF (1996) Electron energy-loss spectroscopy in the electron microscope. Plenum, New York, 2nd edn, pp 301–312

Ford CE, Russel DG, Craven JA, Fisk MR (1983) Olivine–liquid equilibria: temperature, pressure and composition dependence of the crystal/liquid cation partition coefficients for Mg, Fe^{2+}, Ca and Mn. J Petrol 24: 256–265

Franz L, Becker KP, Kramer W, Herzig PM (2000) Metasomatic mantle xenoliths from the Bismarck microplate (Papua New Guinea) – petrological and geochemical consequences and extent of slab-induced hydrous metasomatism. J Petrol (submitted)

Green HW (1985) Coupled exsolution of fluid and spinel from olivine; evidence for O^- in the mantle? In: Schock RN (ed) Point defects in minerals. Geophys Monogr 31: 226–232

Green HW, Gueguen Y (1983) Deformation of peridotite in the mantle and extraction by kimberlite; a case history documented

by fluid and solid precipitates in olivine. In: Etheridge MA, Cox SF (eds) Deformation processes in tectonics. Tectonophysics 92: 71–92
Haggerty SE (1988) Upper mantle opaque mineral stratigraphy and the genesis of metasomatites and alkali-rich melts. J Geol Soc Aust 14: 687–699
Harte B (1977) Rock nomenclature with particular relation to deformation and recrystallization textures in olivine-bearing xenoliths. J Geol 85: 279–288
Herzig PM, Hannington MD, McInnes B, Stoffers P, Villinger H, Seifert R, Binns R, Liebe T, Scientific party R/V SONNE CRUISE SO-94 (1994) Submarine volcanism and hydrothermal venting studied in Papua, New Guinea. Eos, Trans Am Geophys Union 75: 513–516
Herzig PM, Hannington MD, Stoffers P, Becker K-P, Drischel M, Franklin J, Franz L, Gemmel JB, Hoeppner B, Horn C, Horz K, Jellineck T, Jonasson IR, Kia P, Nickelsen S, Percival J, Perfit M, Petersen S, Schmidt M, Seifert T, Thießen O, Türkay M, Tunnicliffe V, Winn K (1998) Petrology, gold mineralization and biological communities at shallow submarine volcanoes of the New Ireland fore-arc (Papua-New Guinea): preliminary results of R/V Sonne cruise SO-133. Inter Ridge News 7: 34–38
Houseman G (1983a) The deep structure of ocean ridges in a convecting mantle. Earth Planet Sci Lett 64: 283–294
Houseman G (1983b) Large aspect ratio convection cells in the upper mantle. Geophys J R Astr Soc 75: 309–334
Houseman G, McKenzie DP (1982) Numerical experiments on the onset of convecting instability in the Earth's mantle. Geophys J R Astr Soc 68: 133–164
Jarosewich E, Nelen JA, Norberg JA (1980) Reference samples for electron microprobe analysis. Geostandard Newslett 4: 43–47
Kennedy AK, Hart SR, Frey FA (1990) Composition and isotopic constraints on the petrogenesis of alkaline arc lavas: Lihir island, Papua New Guinea. J Geophys Res 95: 6929–6942
Kepezhinskas PK, Defant MJ, Drummond MS (1995) Na metasomatism in the island-arc mantle by slab melt-peridotite interaction: evidence from mantle xenoliths in the North Kamchatka arc. J Petrol 36: 1505–1527
Köhler T (1989) Der Ca-Gehalt von Olivin im Gleichgewicht mit Clinopyroxen als Geothermometer. PhD Thesis, University of Mainz
Licence PS, Terril JE, Fergusson LJ (1987) Epithermal gold mineralisation, Ambittle Island, Papua New Guinea. Proc Pacific Rim Conf '87, Australian Institute of Mining and Metallurgy, Melbourne, pp 273–278
Lindsley DH (1983) Pyroxene thermometry. Am Mineral 68: 477–493
Markl G, Marks M, Wirth R (2000) The influence of T, a_{SiO_2} and f_{O_2} on exsolution textures in Fe–Mg olivine: an example from augite syenites of the Ilimaussaq Intrusion, South Greenland. Am Mineral (in press)
McInnes BIA (1992) A glimpse of ephemeral subduction zone processes from Simberi island, Papua New Guinea. PhD Thesis, University of Ottawa, 235 pp
McInnes BIA, Cameron EM (1994) Carbonated, alkaline metasomatic melts from a sub-arc environment: mantle wedge samples from the Tabar–Lhir–Feni arc, Papua New Guinea. Earth Planet Sci Lett 122: 125–141
McInnes BIA, McBride JS, Evans NJ, Lambert DD, Andrew AS (1999) Osmium isotope constraints on ore metal recycling in subduction zones. Science 286: 512–517
McInnes BIA, Gregoire M, Binns RA, Herzig PM, Hannington MD (2000) Hydrous metasomatism of the New Ireland arc mantle xenoliths. Part 1: Petrology and geochemistry of fluid-metasomatized peridotite. Earth Planet Sci Lett (in press)
Mikouchi T, Takeda H, Miyamoto M, Oshumi K, McKay G (1995) Exsolution lamellae of kirschsteinite in magnesium-iron olivine from angrite meteorite. Am Mineral 80: 585–592
Moseley D (1984) Symplectitic exsolution in olivine. Am Mineral 69: 139–153
Mukhopadhyay B (1991) Garnet breakdown in some deep-seated garnetiferous xenoliths from the central Sierra Nevada: petrologic and tectonic implications. Lithos 27: 59–78
Pasteris JD (1983) Spinel zoning in the De Beers kimberlite, South Africa: possible role of phlogopite. Can Mineral 21: 41–58
Puga E, Ruiz Cruz MD, De Federico AD (1999) Magnetite–silicate inclusions in olivine of ophiolitic metagabbros from the Mulhacen complex, Betic Cordillera, southeastern Spain. Can Mineral 37: 1191–1209
Putnis A (1979) Electron photography of high temperature oxidation of olivine from the Rhum layered intrusion. Mineral Mag 43: 293–296
Rabinowicz M, Nicolas A, Vigneresse JL (1984) A rolling mill effect in asthenosphere beneath oceanic spreading centers. Earth Planet Sci Lett 67: 97–108
Rytuba JJ, McKee EH, Cox D (1993) Geochronology and geochemistry of the Ladolam gold deposit, Lihir Island, and gold deposits and volcanoes of Tabar and Tatau, Papua New Guinea. US Geol Surv Bull 2039, pp 119–126
Steward WD, Sandy MJ (1988) Geology of New Ireland and Djaul Islands, northeast Papua New Guinea. In: Marlow MS, Dadisman SV, Exton NF (eds) Geology and offshore resources of Pacific island arcs – New Ireland and Manus region, Papua New Guinea. Circum Pacific Council for Energy and Mineral Resources, Earth Science Series 9, Houston, pp 12–30
Taylor B (1979) Bismarck Sea: evolution of a back arc basin. Geology 7: 171–174
Wagner C, Velde D (1987) Aluminous spinel in lamproites: occurrence and probable significance. Am Mineral 72: 689–696
Wallace DA, Johnson RW, Chappel BW, Arculus RJ, Perfit MR, Crick IH (1983) Cainozoic volcanism of the Tabar-Lihir, Tanga and Feni islands, Papua New Guinea. Rep Bureau Miner Resources Geol Geophys (Aust), vol 243, pp 1–59
Zhang RY, Cong BL, Ying YP, Li JL (1981) Ferrifayallite-bearing eulysite from Archean granulites in Qianan county, Hebei, North China. Tschermaks Mineral Petrogr Mitt 28: 167–187
Zhang RY, Su JF, Mao HK, Liou JG (1999) Magnetite lamellae in olivine and clinohumite from Dabie UHP ultramafic rocks, central China. Am Mineral 84: 564–569